Nanoscale magnetization inhomogeneity within single phase nanopillars

Thomas O. Farmer,[1,2,*] Er-Jia Guo,[1,3] Ryan D. Desautels,[1,4] Lisa DeBeer-Schmitt,[1] Aiping Chen,[5] Zhongchang Wang,[6] Quanxi Jia,[7,8] Julie A. Borchers,[9] Dustin A. Gilbert,[9,10] Ben Holladay,[11] Sunil K. Sinha,[11] and Michael R. Fitzsimmons[1,12,†]

[1]*Neutron Scattering Division, Oak Ridge National Laboratory, Oak Ridge, Tennessee 37831, USA*
[2]*ISIS Neutron and Muon Source, STFC Rutherford Appleton Laboratory, Didcot, OX11 0QX, United Kingdom*
[3]*Beijing National Laboratory for Condensed Matter Physics and Institute of Physics, Chinese Academy of Sciences, Beijing 100190, China*
[4]*Seagate Technology, 1 Disc Drive, Derry, BT48 0BF, United Kingdom*
[5]*Center for Integrated Nanotechnologies (CINT), Los Alamos National Laboratory, Los Alamos, New Mexico 87545, USA*
[6]*Department of Quantum and Energy Materials, International Iberian Nanotechnology Laboratory, Braga 4715-330, Portugal*
[7]*Department of Materials Design and Innovation, University at Buffalo, Buffalo, New York 14260-5030, USA*
[8]*Department of Physics, Konkuk University, Seoul, 05029, Republic of Korea*
[9]*NIST Center for Neutron Research, National Institute of Standards and Technology, Gaithersburg, Maryland 20899, USA*
[10]*Department of Materials Science and Engineering, University of Tennessee, Knoxville, Tennessee 37919, USA*
[11]*Department of Physics, University of California, San Diego, La Jolla, California 92093-0319, USA*
[12]*Department of Physics and Astronomy, University of Tennessee, Knoxville, Tennessee 37996, USA*

We report observation of a radial dependence in the magnetic anisotropy of epitaxially strained $CoFe_2O_4$ nanopillars in a $BaTiO_3$ matrix. This archetypal example of a multiferroic heterostructure with a self-assembling three-dimensional architecture possesses significant out-of-plane uniaxial magnetic anisotropy. The anisotropy originates from the large magnetostriction of $CoFe_2O_4$ and the state of stress within the nanocomposite. Magnetometry suggests the existence of two magnetic phases with different anisotropies. Micromagnetic simulations of a core-shell magnetic anisotropy qualitatively reproduce features of the magnetic hysteresis and elucidate the magnetization reversal mechanism: The magnetization initially reorients within the pillar core, followed by that of the shell. This is consistent with polarized small-angle neutron scattering which can be described by a $CoFe_2O_4$ magnetization that is nonuniform on nanometer length scales. As the length scale of inhomogeneity of the magnetic anisotropy is similar to estimates of the relaxation of the displacement field from the $CoFe_2O_4$-$BaTiO_3$ interface, stress and its influence on structure provide an important route to new functionality of vertically aligned nanopillars for applications in low-power memory, computing, and sensing.

Recently there has been growing interest in multiferroic materials [1–4] due to the intriguing physics that is inherent in the coupled order parameters that they possess [5,6], which may enable novel memory and sensor applications [7,8]. Presently, single phase multiferroics, particularly those with ferromagnetic (FM) and ferroelectric (FE) order parameters, do not possess large magnetoelectric coupling [9,10]. Thus, an alternative approach of using heterostructures, i.e., nanocomposites, consisting of materials with different ferroic orders, has been pursued [4,11–14].

For thin-film multiferroic heterostructures, often the magnitude of the multiferroic response depends on the interfacial area; binary two-dimensional (2D) films are limited by the extent to which this propagates from the interface [9,15]. By contrast, for three-dimensional (3D) architectures such as vertically aligned nanopillars (VANs), the interfacial area scales with film thickness, pillar diameter, and density [4,11,16–19]. This means coupling of, for example, magnetic and elec-

tric order parameters (magnetoelectric coupling) may remain strong even in thick films. As the variation of atomic structure (commonly referred to as strain) within these structures is determined by the competition between the substrate and out-of-plane interfaces, this geometry also enables strain control [16,19], compared with 2D films which are only controlled by substrate clamping [20]. These properties have motivated significant research into 3D architectures for multiferroic heterostructures and beyond [19,21–24].

Nanopillars of ferromagnetic spinel $CoFe_2O_4$ (CFO) within a ferroelectric perovskite $BaTiO_3$ (BTO) matrix are a prototypical example of a VAN multiferroic, due to the large magnetostriction of CFO [25] and ferroelectric response of BTO [26]. This system and comparable crystal structures are amenable to heteroepitaxial growth along the normal to the film's surface, i.e., vertical direction [11]. Lattice mismatch between the CFO and BTO causes interfacial strain. The strain induces a large out-of-plane uniaxial magnetic anisotropy in the CFO [4,27,28]. Due to the sensitivity of the anisotropy to strain, even slight relaxation within the CFO pillars can cause significant changes to the magnetic behavior. Consequently, relaxation of the displacement field away from the interface,
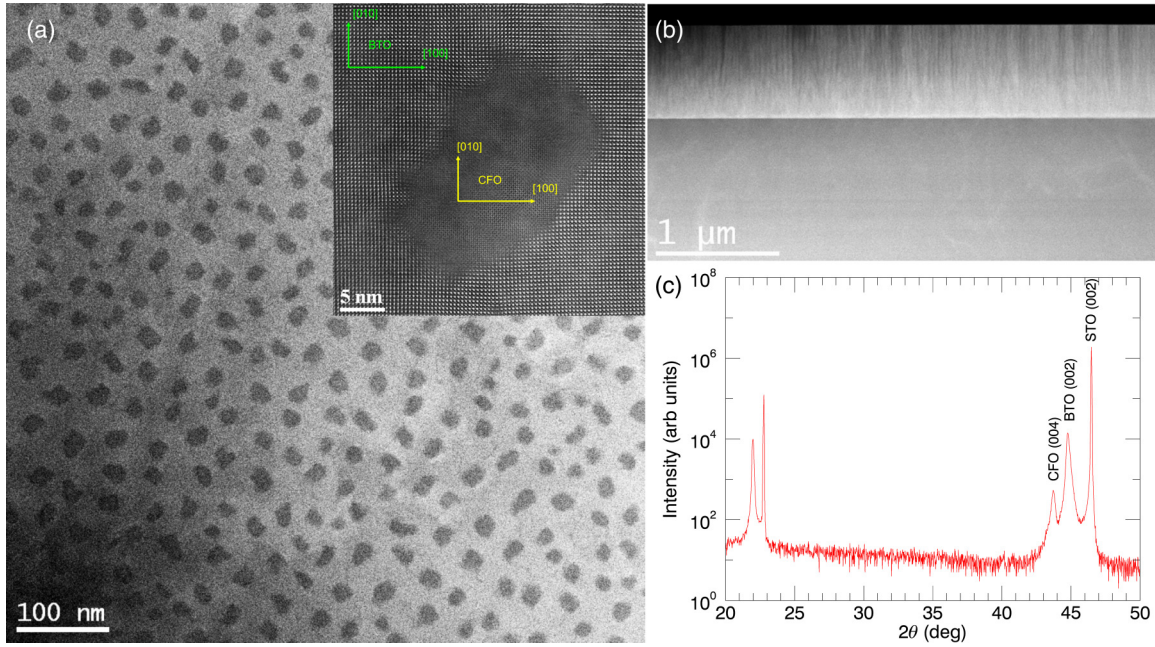
*tom.farmer@stfc.ac.uk
†fitzsimmonsm@ornl.gov

FIG. 1. (a) Plan view and (b) cross-sectional HAADF STEM showing the sample morphology and thickness of a 720-nm BTO-CFO VAN grown on 30-nm SRO buffered STO(001). Inset: Epitaxial relationship between a single CFO pillar and the surrounding BTO matrix. (c) X-ray diffractogram ($\theta - 2\theta$ scan) of the BTO-CFO nanocomposite film.

often reported in lateral heterostructures [29,30], could produce a nonuniform magnetic field dependence of the magnetization within a VAN—although this is presently unknown. In order to maximize the magnetoelectric coupling, knowledge of the spatial dependence of the magnetic anisotropy is essential. Here we report on a combined study of micromagnetic simulation, magnetometry, and polarized small-angle neutron scattering (SANS). The micromagnetic simulation demonstrates that a CFO nanopillar with a high anisotropy shell and a lower anisotropy core is required to describe the field dependence of the magnetization. Polarized beam SANS data measured away from saturation are consistent with the nanopillars possessing a nonuniform distribution of magnetization.

Samples were grown using pulsed laser deposition from a $(BaTiO_3)_{0.65}(CoFe_2O_4)_{0.35}$ (molar ratio) composite target with a substrate temperature of $850\,°C$, an oxygen pressure of 50 mTorr (1 Torr = 133 Pa), and a laser energy of $2\,J/cm^2$, consistent with previous reports [4,11]. Film thicknesses of 720 nm were deposited on (001) Nb:SrTiO$_3$ (Nb:STO, Nb doping, 0.7%) and STO (001) substrates [Figs. 1(a) and 1(b)]. A bottom electrode SrRuO$_3$ (SRO) with a layer thickness of 30 nm was grown on STO by pulsed laser deposition. Epitaxial growth of CFO nanopillars of an average diameter of 18(2) nm and a volume fraction of 0.17(2) is evidenced by high-angle annular dark field scanning transmission electron microscopy (HAADF-STEM) images [Fig. 1(a)] (detailed in the Supplemental Material [31]). X-ray diffraction (XRD), performed using a Cu $K\alpha$ (1.5406 Å) source, indicates no impurity phases and establishes the BTO and CFO c axis parameters to be 4.045(2) Å and 8.277(4) Å, respectively [Fig. 1(c)]; the CFO is 1.4% compressively strained in the out-of-plane direction relative to the bulk lattice parameter [32] (8.392 Å). Previously, single phase CFO films on STO substrates were shown to have out-of-plane tensile strain

[33]. The large out-of-plane compressive strain of the CFO nanopillars is dominated by the vertical interface coupling rather than the STO substrate [34].

Superconducting quantum interference device (SQUID) magnetometry (Fig. 2) performed at 300 K shows a significant perpendicular magnetic anisotropy between the in-plane and out-of-plane directions, along with a kink at low field, which is consistent with previous BTO-CFO VAN magnetic hysteresis loops [4,27]. The magnetization of 400(30) kA/m, which was normalized to the volume fraction of the CFO determined from STEM, is somewhat lower than the bulk value of 477 kA/m or $3.65\,\mu_B/f.u.$ [35]. As the CFO spinel inversion is strongly dependent on the growth conditions [36], and the theoretical magnetic moment for a completely inverse CoFe$_2$O$_4$ spinel is $3\,\mu_B/f.u.$ [37], the decreased magnetization of our samples may originate from a higher distribution
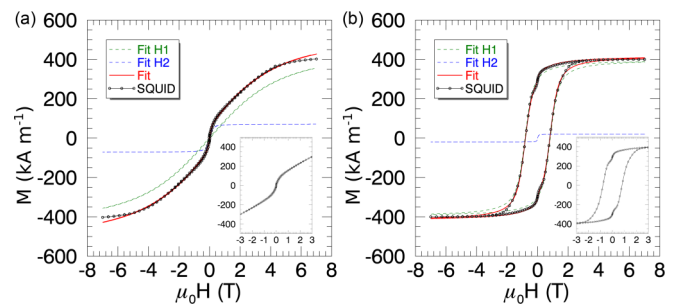

FIG. 2. (a) In-plane and (b) out-of-plane magnetic hysteresis loops (black curve and circles) with fits to the data (red curve) and the components of fits (dashed curves). H1 and H2 denote the two hysteresis loops. The insets highlight the shape of the experimental MH loops at small fields. The error bars are smaller than the symbol size.
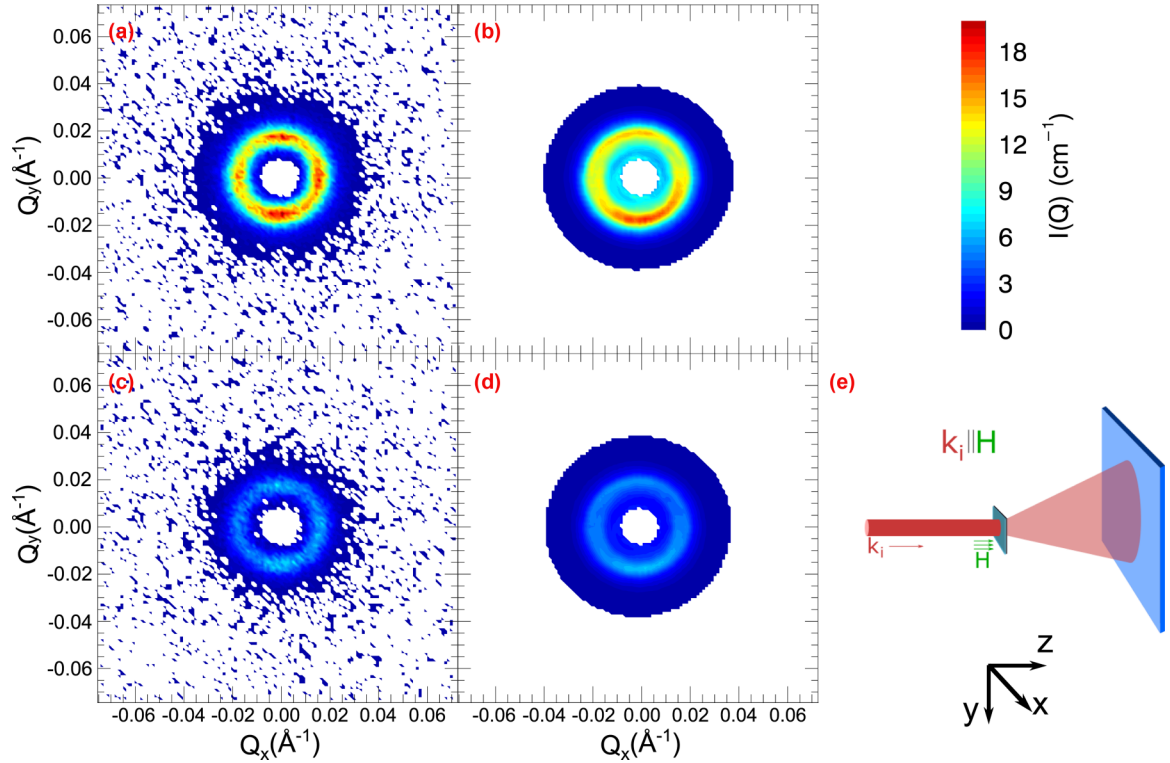
FIG. 3. SANS with polarized neutron beam for $+7$ mT and model fit: (a),(b) $I^+(Q)$, (c),(d) $I^-(Q)$. The ring feature is identified at $Q = 0.0168$ Å^{-1}. (e) Schematic of neutron experiment. The final wave vector k_f lies inside the cone. The scattering vector Q lies in the green colored plane at the position of the sample.

of Co^{2+} in octahedral sites. Another potential cause is spin disorder at vertical interfaces, which is commonly posited as an explanation for reduced magnetization in nanopillars [38].

The MH loops can be fitted by a minimum of two hysteresis loops (Fig 2), representing different fractions of hard and soft magnetic phases. This is congruent with reports of exchange coupled FePt/Fe$_3$O$_4$ nanoparticles [39], where similar behavior was attributed to an incomplete coupling between the soft and hard magnetic phases arising from two different chemical phases. However, for the BTO-CFO VAN, the two magnetic responses originate from a *single chemical phase* of ferromagnetic material. There is a significant difference in the saturation magnetization M_s of the soft magnetic hysteresis loop for fields applied in and out of the sample plane. These differences suggest the two magnetic phases are partially coupled, potentially originating from a nonuniform lateral magnetization within the nanopillars, which motivates the SANS study.

From the in-plane MH loop an anisotropy field [40], H_k, of 6.5 T can be estimated. Assuming magnetostriction is dominant, the anisotropy field H_k is related to the CFO strain in the [001] direction ε_{001} by $H_k = -3\lambda_{001}\Upsilon\varepsilon_{001}$, where λ_{001} is the magnetostriction in the [001] direction and Υ is the Young's

modulus of CFO. However, while values of the CFO Young's modulus are relatively consistent [32,41,42], there is significant variation in the literature values of λ_{001} [25,41,43,44] [$(250-600) \times 10^{-6}$], which has also been reported to have a strong dependence on the degree of spinel inversion [45]. Therefore, given the measurements of H_k [from Fig. 2(b)] and ε_{001} (from XRD) and the literature value of 141.6 GPa for Υ, our value of $\lambda_{001} = 340 \times 10^{-6}$ is consistent with the reported range.

SANS with a polarized incident beam was conducted on NG7 at NIST (Fig. 3) on two samples placed face to face, with the pillars parallel to the incident beam and the neutron beam polarization. Due to the large anisotropy field, these samples were saturated with a $+7$ T out-of-plane field *ex situ* and then measured at $+7$ mT (near remanence) and -500 mT field where the sign is taken with respect to the saturation field. Neutron scattering is sensitive to the magnetization that is perpendicular to the scattering wave vector, $\vec{Q} = (\vec{k}_f - \vec{k}_i)$ (the difference between the wave vectors of the incident and scattered neutron beam, k_i, and k_f, respectively, equals $4\pi\sin(\psi)/\lambda_n$, where 2ψ is the angle between k_i, and k_f [half the cone angle in Fig. 3(e)] and λ_n is the wavelength). The intensity of the neutron scattering for each polarization state of the incident beam for our experiment is [46]:

$$I^\pm(Q) = \frac{8\pi^3}{V}\left(\begin{array}{c}|\widetilde{N}|^2 + b_H^2|\widetilde{M}_z|^2 \mp b_H(\widetilde{N}\widetilde{M}_z{}^* + \widetilde{N}^*\widetilde{M}_z) + b_H^2|\widetilde{M}_y|^2\cos\theta \\ +b_H^2|\widetilde{M}_x|^2\sin\theta - b_H^2(|\widetilde{M}_x||\widetilde{M}_y{}^*| + |\widetilde{M}_x{}^*||\widetilde{M}_y|)\sin\theta\cos\theta\end{array}\right), \qquad (1)$$

TABLE I. SANS fit results for 7 and −500 mT applied fields.

Applied field (mT)	7	−500
Core SLD (10^{-6} Å^{2})	−0.19 (2)	−0.42 (7)
Shell SLD (10^{-6} Å^{2})	1.0 (1)	1.1 (1)
Core radius (nm)	3.7 (4)	4.4 (7)
Shell thickness (nm)	7.1 (6)	6.4 (9)
Core polydispersity (nm)	0.18 (4)	0.18 (6)
Shell polydispersity (nm)	0.09 (2)	0.08 (3)
Roughness (nm)	7 (1)	6.1 (8)

TABLE II. Input parameters for micromagnetics simulations of a single CFO cylinder. A value for the exchange constant within the range of previously reported values [54,55] was used.

Cell size (nm)	0.5
Core diameter (nm)	7
Shell thickness	5
Cylinder height (nm)	36
A, Exchange constant (J/m)	13×10^{-13}
Shell uniaxial anisotropy (J/m^{3})	6×10^{5}
Field step size (mT)	20
Saturation magnetization (kA/m)	400

where θ is the angle between the x axis [Fig. 3(e)] and $\vec{Q}$, and V is the volume; $\tilde{N}$ and $\tilde{M}$ are the spatial Fourier transforms of the nuclear and magnetic scattering length densities (SLDs) respectively, and $b_H = 2.91 \times 10^8 \, \mathrm{A^{-1} \, m^{-1}}$ is a constant relating the atomic magnetic moment to the Bohr magneton [46]. As the magnetometry shows that the z component of the magnetization is significantly larger than the in-plane components, the difference between the polarization states [defined by $\mp$ in (1)] is predominantly a measure of M_z, as a function of x and y.

Standard corrections [47], including accounting for a beam polarization of 93%, were applied to each dataset. From the relative length scales observed with STEM, the ring at $0.0168 \, \text{Å}^{-1}$ (Fig. 3) is due to internanopillar correlations (structure factor), while the high-Q data are more sensitive to the nanopillar size and shape (form factor). The Fourier transform of a 2D model of simulated structures similar to that observed in the STEM was fit to the spin asymmetry, $[I^+(Q) - I^-(Q)]/[I^+(Q) + I^-(Q)]$, as detailed in the Supplemental Material [31] (Figs. S1 and S2).

Roughness (or variation) in the position r of the interface from the axis of the pillar represents the deviation of the CFO/BTO interface from its mean value along the length (i.e., along z) and circumference [i.e., from $\varphi = 0$ to 2π, where $\phi \, (= \theta)$ is the polar angle in the plane of the film]. The roughness is included in the scattering calculation as a Debye-Waller factor of the form [48]:

$$e^{-(Q_x^2 + Q_y^2)G(\varphi,z)/2}, \quad (2)$$

where

$$G(\varphi, z) = \langle [r(\varphi, z) - r(\varphi', z')]^2 \rangle, \quad (3)$$

the roughness factor, is the mean squared difference between the radii of any two points on the surface of the nanopillar and Q_x and Q_y are the components of Q parallel to the plane of the detector.

As models with both uniform and nonuniform magnetic SLDs have similar reduced chi squared values [49], these SANS data are insufficient for differentiating between the two; the large pillar roughness (Table I) obfuscates the details in the form factor. For comparison, the magnitude of the roughness factor $G(\varphi)$, determined from the STEM, is 2.6(5) nm (integrated over a z slice of the film prepared for microscopy). This is potentially indicative of a larger roughness along the pillars than around their radii, although this cannot be confirmed without determining $G(\varphi)$ for several film thicknesses. In the case of the core-shell model, the core

magnetic SLD decreases as the applied field approaches the coercive field from saturation.

In order to distinguish between the two SANS models and elucidate the origin of the magnetization reversal process, we performed micromagnetic simulations using the object oriented micromagnetic framework [50] (OOMMF) on a 48-node cluster. The simulation parameters which provided the best agreement with the magnetometry are shown in Table II, with the cell size (0.5 nm) selected to be smaller than the exchange length [51] (1.5 nm). The maximum angle between adjacent spins, $\delta\omega$ [Fig. 4(b)], controlled by the value of the exchange constant, remained below 16°, except for the coercive field H_c when $\delta\omega$ peaks at 28°; a maximum spin angle of less than 30° usually indicates good reliability of the simulation [52,53]. Simulations reported here were of a single CFO
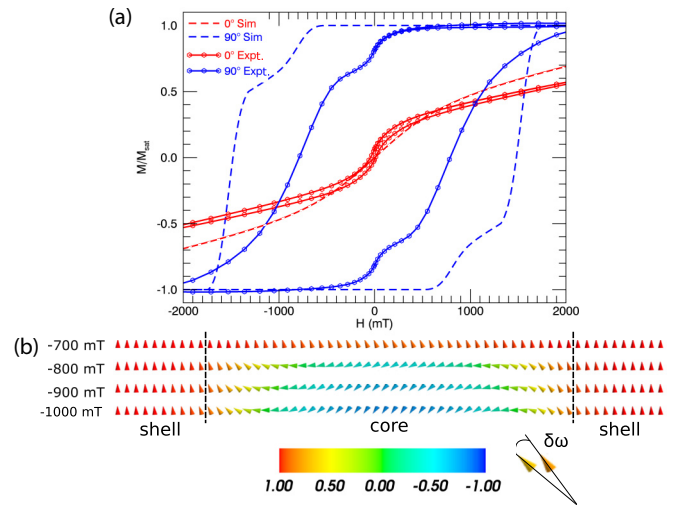

FIG. 4. (a) In-plane (red) and out-of-plane (blue) magnetic hysteresis loops from SQUID (solid curves) and micromagnetic simulations (dashed curves). The simulated MH half loop has been mirrored in x and y for ease of comparison. The error bars are smaller than the symbol size. (b) Distribution of M_z/M_{sat} across the y axis for a single row of cells across the center of the pillar as it switches from $+z$ (red) to $-z$ (blue), for four different fields. The initial saturation was in the $+z$ direction. The dashed lines delineate the boundary between the shell and core cells. The angle between adjacent spins, $\delta\omega$, is depicted.
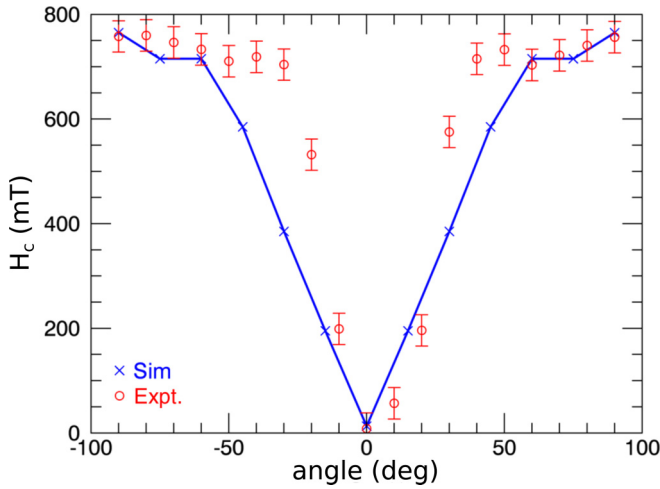
FIG. 5. Angular dependence of the coercivity from SQUID (red circles) and micromagnetic simulations (blue curve with ×), where $0°$ is in plane. The coercivity of the micromagnetic simulations has been scaled to the maximum of the SQUID data.

nanopillar, although comparisons made with simulations of multiple nanopillars were also explored and the interstructure magnetic interactions were found to be weak (Fig. S3 in the Supplemental Material [31]). Periodic boundary conditions were used in the out-of-plane (z) direction, to increase the accuracy of the calculated demagnetization energy; however, the effect of removing this periodicity was negligible. To account for the effect of sample polydispersity on the hysteresis loops, we examined simulations for different size pillars. We found the loop shapes to be similar, but H_c was correlated with pillar diameter, enabling a distribution of radii ($\sigma = 2.0$ nm) to be approximated from the simulation results of the mean radius (Fig. S4 in the Supplemental Material [31]).

Along with assuming that interpillar interactions were negligible, other simplifications were made, including the simulated nanopillar is perfectly cylindrical, normal to the sample plane, and the magnetic anisotropy was divided into two distinct regions (specifically a soft magnetic core and a hard magnetic shell). Despite these simplifications the simulation captures the essential features of the in-plane and out-of-plane magnetometry data [Fig. 4(a)]. Alternative models using a single magnetic region and a hard core/soft shell were unable to reproduce the qualitative agreement. The best agreement was achieved with a larger ratio of core to shell dimensions than that inferred from the SANS fit. This larger ratio was required in order to decrease the strength of the coupling between the two regions; this difference could be due to an overestimation of the shell anisotropy, or related to the idealized cylindrical shape of the simulation, both of which are also likely to be responsible for the larger coercivity of the simulation. The presence of magnetically soft defect sites and thermally activated reversal, both of which were not modeled here, will also limit the ability to quantitatively compare the simulations to the experimental results. Another test of the simulation is to observe how H_c varies with angle relative to the in-plane direction (Fig. 5). The calculated and measured variations of H_c with angle qualitatively agree,

further supporting modeling with two magnetic phases with different anisotropies, despite the simplifications required to make the simulation computationally tractable.

By studying the magnetization distribution within the simulated pillar, it is possible to understand the reversal mechanism, particularly how the interaction between the core and shell regions results in an initial sharp decrease in the magnetization. Figure 4(b) shows the magnetization of each cell in a row representative of the bulk for four different fields, following saturation at $+2000$ mT. At -700 mT both the core and shell spins are largely aligned in opposition to the field. The magnitude of the field is significantly smaller than is required to overcome the uniaxial anisotropy in the shell, and the exchange energy pins the core magnetization. Between -700 and -800 mT the increasing Zeeman energy cost is larger than the additional exchange energy associated with rotating core spins that are not at the core-shell interface, causing the magnetization of the core to rotate by $90°$, moving toward the magnetic field. Further reducing the magnetic field, i.e., making the field more negative, causes the core to continue to rotate toward the applied magnetic field; however, the shell remains pinned in its initial orientation due to its large magnetocrystalline anisotropy. This reversal mechanism is similar to the Wiegand effect [56] which involves introducing a variation of anisotropy by strain induced hardening of the outer shell of a magnetic wire, albeit at the macroscale. Due to the reduced dimensions of the magnetic material, pinning of the interface magnetization plays the dominant role in the macroscopic magnetic properties, e.g., the coercivity, of the nanocomposite. Manipulation of interface pinning using the ferroelectric response of BTO should provide an intriguing means to achieve a multiferroic response.

As has been previously established [4], despite the large aspect ratio of BTO-CFO VAN, if the nanopillars are epitaxially strained then the magnetoelasticity, rather than the demagnetization, is the dominant contribution to the anisotropy energy. A particularly elegant demonstration of this is reported by Wang *et al.* [28], who showed a significant reduction in the anisotropy of CFO nanopillars embedded in a $BiFeO_3$ matrix after the $BiFeO_3$ matrix was etched away.

A potential mechanism for the spatial dependence of the magnetization is relaxation of the displacement field within a magnetostrictive material. Misfit dislocations (MDs) are linear defects (dislocations) that accommodate lattice mismatch across an interface by producing a variation of the displacement field [57]. (We use the term "displacement field" rather than strain, because the latter considers materials in the continuum limit and thus not necessarily appropriate for describing the displacement of atoms in proximity to interfaces such as encountered in nanostructured materials, e.g., nanopillars). An example includes an array (network) of dislocations at the interface between an epitaxial oxide film grown on an oxide substrate [e.g., $La_{(1-x)}Sr_xMnO_3$ film on $LaAlO_3$ substrate (LSMO/LAO)] [58]. The displacement field decays within nanometers to tens of nanometer from the interface depending upon several factors including lattice mismatch, Burgers vectors, chemistry, etc. The decay of the displacement field influences materials properties, including electric and magnetic properties. Santiso *et al.* [59] report estimates of the displacement field using the Matthews-Blakeslee model

[60] for LSMO/LAO of 1.7 nm that is "slightly below" their measurement of 2.5 nm.

The CFO/BTO interfaces parallel to the growth direction break the lateral (in the film plane) symmetry of our nanostructured system. We attribute the nonuniformity of the lateral magnetization to the variation of the displacement field within the magnetostrictive CFO nanopillars. The upper limit of the length scale of the displacement field in the lateral direction is the lateral dimension of the nanopillar, ~ 11 nm. To estimate the lower limit h_c, analogous to the approach of Santiso *et al.* [59], we use the Matthews-Blakeslee equation [60]:

$$h_c = \frac{b}{2\pi f} \frac{(1 - v\cos^2\alpha)}{(1 + v)\cos\lambda} \left(\ln \frac{h_c}{b} + 1 \right), \qquad (4)$$

where b is the magnitude of the Burgers vector, f is the bulk lattice mismatch, v is Poisson's ratio, α is the angle between the dislocation line and its Burgers vector, and λ is the angle between the slip direction and the Burgers vector. Taking $f = 0.038$, $v = 0.26$ [61], $b = 4.195$ Å, $\alpha = \pi/2$, and $\lambda = 0$ [62], $h_c \sim 5$ nm, which is comparable to the shell thicknesses obtained from micromagnetic simulations and SANS. We expect variation of the displacement field toward the center of a pillar of a magnetostrictive material like the CFO will produce nonuniform magnetization and the length scales of the displacement field and magnetic nonuniformity will be related.

In summary, we have demonstrated a BTO-CFO VAN with concomitant nonuniform magnetic anisotropy, which is of comparable length scale to the theoretical onset of relaxation of the displacement field. As similar two phase magnetic behavior has been inferred from magnetometry in other FM VAN systems [18,27,63,64], the magnetization reversal mechanism identified for the BTO-CFO nanocomposite may be generally applicable to many VAN systems with large magnetostriction. As both nanopillar size [64] and interfacial strain [16] can be controlled and our simulations indicate such control enables tuning of H_c, establishing this mechanism is a significant step toward tailoring the magnetic response, and the magnetoelectric coupling, in 3D heterogeneous architectures.

[1] W. Eerenstein, N. D. Mathur, and J. F. Scott, Nature **442**, 759 (2006).

[2] J. Wang, J. B. Neaton, H. Zheng, V. Nagarajan, S. B. Ogale, B. Liu, D. Viehland, V. Vaithyanathan, D. G. Schlom, U. V Waghmare, N. A. Spaldin, K. M. Rabe, M. Wuttig, and R. Ramesh, Science **299**, 1719 (2003).

[3] C. W. Nan, M. I. Bichurin, S. Dong, D. Viehland, and G. Srinivasan, J. Appl. Phys. **103**, 031101 (2008).

[4] H. Zheng, J. Wang, S. E. Lofland, Z. Ma, L. Mohaddes-Ardabili, T. Zhao, L. Salamanca-Riba, S. R. Shinde, S. B. Ogale, F. Bai, D. Viehland, Y. Jia, D. G. Schlom, M. Wuttig, A. Roytburd, and R. Ramesh, Science **303**, 661 (2004).

[5] N. A. Hill, J. Phys. Chem. B **104**, 6694 (2000).

[6] I. A. Sergienko and E. Dagotto, Phys. Rev. B **73**, 094434 (2006).

[7] J. F. Scott, Nat. Mater. **6**, 256 (2007).

[8] S. M. Wu, S. A. Cybart, P. Yu, M. D. Rossell, J. X. Zhang, R. Ramesh, and R. C. Dynes, Nat. Mater. **9**, 756 (2010).

[9] L. W. Martin, S. P. Crane, Y. H. Chu, M. B. Holcomb, M. Gajek, M. Huijben, C. H. Yang, N. Balke, and R. Ramesh, J. Phys.: Condens. Matter **20**, 434220 (2008).

[10] C. A. F. Vaz, J. Hoffman, C. H. Ahn, and R. Ramesh, Adv. Mater. **22**, 2900 (2010).

[11] H. Zheng, J. Wang, L. Mohaddes-Ardabili, M. Wuttig, L. Salamanca-Riba, D. G. Schlom, and R. Ramesh, Appl. Phys. Lett. **85**, 2035 (2004).

[12] C. Deng, Y. Zhang, J. Ma, Y. Lin, and C. W. Nan, J. Appl. Phys. **102**, 074114 (2007).

[13] Y. Chen, T. Fitchorov, C. Vittoria, and V. G. Harris, Appl. Phys. Lett. **97**, 052502 (2010).

[14] F. Zavaliche, H. Zheng, L. Mohaddes-Ardabili, S. Y. Yang, Q. Zhan, P. Shafer, E. Reilly, R. Chopdekar, Y. Jia, P. Wright, D. G. Schlom, Y. Suzuki, and R. Ramesh, Nano Lett. **5**, 1793 (2005).

[15] M. I. Bichurin, V. M. Petrov, and G. Srinivasan, Phys. Rev. B **68**, 054402 (2003).

[16] J. L. MacManus-Driscoll, P. Zerrer, H. Wang, H. Yang, J. Yoon, A. Fouchet, R. Yu, M. G. Blamire, and Q. X. Jia, Nat. Mater. **7**, 314 (2008).

[17] W. Zhang, J. Jian, A. Chen, L. Jiao, F. Khatkhatay, L. Li, F. Chu, Q. X. Jia, J. L. MacManus-Driscoll, and H. Wang, Appl. Phys. Lett. **104**, 062402 (2014).

[18] L. Shen, C. Ma, S. Cheng, S. Ren, S. Cheng, S. Mi, and M. Liu, J. Mater. Chem. C **4**, 10955 (2016).

[19] A. Chen, J.-M. Hu, P. Lu, T. Yang, W. Zhang, L. Li, T. Ahmed, E. Enriquez, M. Weigand, Q. Su, H. Wang, J.-X. Zhu, J. L. MacManus-Driscoll, L.-Q. Chen, D. Yarotski, and Q. X. Jia, Sci. Adv. **2**, e1600245 (2016).

[20] A. L. Kholkin, E. K. Akdogan, A. Safari, P. F. Chauvy, and N. Setter, J. Appl. Phys. **89**, 8066 (2001).

[21] S. A. Harrington, J. Y. Zhai, S. Denev, V. Gopalan, H. Y. Wang, Z. X. Bi, S. A. T. Redfern, S. H. Baek, C. W. Bark, C. B. Eom, Q. X. Jia, M. E. Vickers, and J. L. MacManus-Driscoll, Nat. Nanotechnol. **6**, 491 (2011).

[22] A. P. Chen, Z. X. Bi, Q. X. Jia, J. L. MacManus-Driscoll, and H. Y. Wang, Acta Mater. **61**, 2783 (2013).

[23] W. Zhang, A. Chen, Z. Bi, Q. X. Jia, J. L. MacManus-Driscoll, and H. Wang, Curr. Opin. Solid State Mater. Sci. **18**, 6 (2014).

[24] J. Huang, J. L. MacManus-Driscoll, and H. Wang, J. Mater. Res. **32**, 4054 (2017).

[25] R. M. Bozorth and J. G. Walker, Phys. Rev. **88**, 1209 (1952).

[26] K. J. Choi, M. Biegalski, Y. L. Li, A. Sharan, J. Schubert, R. Uecker, P. Reiche, Y. B. Chen, X. Q. Pan, V. Gopalan, L.-Q. Chen, D. G. Schlom, and C. B. Eom, Science **306**, 1005 (2004).

[27] N. M. Aimon, D. Hun Kim, H. Kyoon Choi, and C. A. Ross, Appl. Phys. Lett. **100**, 092901 (2012).

[28] Z. Wang, R. Viswan, B. Hu, V. G. Harris, J.-F. Li, and D. Viehland, Phys. Status Solidi RRL **6**, 92 (2012).

[29] Y. Wang, S. G. Kim, and I-W. Chen, Acta Metall. **56**, 5312 (2008).

[30] J. Gazquez, S. Bose, M. Sharma, M. A. Torija, S. J. Pennycook, C. Leighton, and M. Varela, APL Mater. **1**, 012105 (2013).

[31] See Supplemental Material at http://link.aps.org/supplemental/10.1103/PhysRevMaterials.3.081401 for details on the TEM and STEM characterization, SANS analysis, and micromagnetic simulations of multiple nanopillars and nanopillars of varying diameters. See Refs. [65–67].

[32] Z. Li, E. S. Fisher, J. Z. Liu, and M. V. Nevitt, J. Mater. Sci. **26**, 2621 (1991).

[33] W. Huang, L. X. Zhou, H. Z. Zeng, X. H. Wei, J. Zhu, Y. Zhang, and Y. R. Li, J. Cryst. Growth **300**, 426 (2007).

[34] A. Chen, Q. Su, H. Han, E. Enriquez, and Q. X. Jia, Adv. Mater. **31**, 1803241 (2019).

[35] W. H. Wang and X. Ren, J. Cryst. Growth **289**, 605 (2006).

[36] S. Trolier-McKinstry and R. E. Newnham, *Materials Engineering Bonding, Structure, and Structure-Property Relationships* (Cambridge University Press, Cambridge, 2018), p. 551.

[37] Y. H. Hou, Y. J. Zhao, Z. W. Liu, H. Y. Yu, X. C. Zhong, W. Q. Qiu, D. C. Zeng, and L. S. Wen, J. Phys. D: Appl. Phys. **43**, 445003 (2010).

[38] R. H. Kodama, J. Magn. Magn. Mater. **200**, 359 (1999).

[39] H. Zeng, J. Li, J. P. Liu, Z. L. Wang, and S. Sun, Nature **420**, 395 (2002).

[40] B. D. Cullity, *Introduction to Magnetic Materials* (Addison-Wesley, Reading, MA, 1972).

[41] R. M. Bozorth, E. F. Tilden, and A. J. Williams, Phys. Rev. **99**, 1788 (1955).

[42] V. A. M. Brabers, in *Landolt-Börnstein, Group III, Condensed Matter, Vol. 27D Oxy-Spinels*, edited by H. P. J. Wijn (Springer-Verlag, Berlin, Heidelberg, 1991).

[43] M. Abes, C. T. Koops, S. B. Hrkac, J. McCord, N. O. Urs, N. Wolff, L. Kienle, W. J. Ren, L. Bouchenoire, B. M. Murphy, and O. M. Magnussen, Phys. Rev. B **93**, 195427 (2016).

[44] V. J. Folen, in *Landolt-Börnstein, Group III, Condensed Matter, Vol. 4B, Part B*, edited by K.-H. Hellwege and A. M. Hellwege (Springer-Verlag, Berlin, Heidelberg, 1970).

[45] I. C. Nlebedim, N. Ranvah, P. I. Williams, Y. Melikhov, J. E. Snyder, A. J. Moses, and D. C. Jiles, J. Magn. Magn. Mater. **322**, 1929 (2010).

[46] A. Michels, J. Phys.: Condens. Matter **26**, 383201 (2014).

[47] S. R. Kline, J. Appl. Crystallogr. **39**, 895 (2006).

[48] S. K. Sinha, E. B. Sirota, S. Garoff, and H. B. Stanley, Phys. Rev. B **38**, 2297 (1988).

[49] P. R. Bevington and D. K. Robinson, *Data Reduction and Error Analysis for the Physical Sciences* (McGraw-Hill, New York, 1992).

[50] M. J. Donahue and D. G. Porter, OOMMF User's Guide, Version 1.0 (Gaithersburg, MD, 1999).

[51] G. S. Abo, Y. K. Hong, J. Park, J. Lee, W. Lee, and B. C. Choi, IEEE Trans. Magn. **49**, 4937 (2013).

[52] M. Pohlit, I. Stockem, F. Porrati, M. Huth, C. Schröder, and J. Müller, J. Appl. Phys. **120**, 142103 (2016).

[53] A. Vansteenkiste, J. Leliaert, M. Dvornik, M. Helsen, F. Garcia-Sanchez, and B. Van Waeyenberge, AIP Adv. **4**, 107133 (2014).

[54] N. M. Aimon, J. Liao, and C. A. Ross, Appl. Phys. Lett. **101**, 232901 (2012).

[55] M. Y. Rafique, L. Pan, Q. Javed, M. Z. Iqbal, and L. Yang, J. Nanopart. Res. **14**, 1189 (2012).

[56] H. E. Burke, *Handbook of Magnetic Phenomena* (Van Nostrand Reinhold Company, New York, 1986).

[57] F. Sandiumenge, Front. Mater. **6**, 13 (2019).

[58] F. Sandiumenge, N. Bagués, J. Santiso, M. Paradinas, A. Pomar, Z. Konstantinovic, C. Ocal, L. Balcells, M.-J. Casanove, and B. Martínez, Adv. Mater. Interfaces **3**, 1600106 (2016).

[59] J. Santiso, J. Roqueta, N. Bagués, C. Frontera, Z. Konstantinovic, Q. Lu, B. Yildiz, B. Martínez, A. Pomar, L. Balcells, and F. Sandiumenge, ACS Appl. Mater. Interfaces **8**, 16823 (2016).

[60] J. W. Matthews and A. E. Blakeslee, J. Cryst. Growth **27**, 118 (1974).

[61] S. R. Murthy, Phys. Status Solidi **80**, K161 (1983).

[62] A. K. Axelsson, F. Aguesse, L. Spillane, M. Valant, D. W. McComb, and N. M. Alford, Acta Mater. **59**, 514 (2011).

[63] H. J. Liu, L. Y. Chen, Q. He, C. W. Liang, Y. Z. Chen, Y. S. Chien, Y. H. Hsieh, S. J. Lin, E. Arenholz, C. W. Luo, Y. L. Chueh, Y. C. Chen, and Y. H. Chu, ACS Nano **6**, 6952 (2012).

[64] W. Zhang, M. Fan, L. Li, A. Chen, Q. Su, Q. X. Jia, J. L. MacManus-Driscoll, and H. Wang, Appl. Phys. Lett. **107**, 212901 (2015).

[65] H. Zheng, Dissertation, Growth and characterization of multi-ferroic BaTiO$_3$-CoFe$_2$O$_4$ thin film nanostructures, University of Maryland, 2004.

[66] J. Moré, Numerical Analysis, in *Proceedings of 11th Biennial Conference, Dundee*, edited by G. A. Watson (Springer-Verlag, Berlin, 1977), Vol. 630, p. 105.

[67] C. B. Markwardt, in *Astronomical Data Analysis Software and Systems XVIII*, ASP Conference Series, edited by D. A. Bohlender, D. Durand, and P. Dowler (Astronomical Society of the Pacific, San Francisco, 2009), Vol. 411, p. 251.

[68] http://energy.gov/downloads/doe-public-access-plan.